Lattice dynamics and metastability of fcc metals in the hcp structure and the crucial role of spin-orbit coupling in platinum

Stephan Schönecker,[1,*] Xiaoqing Li,[1,†] Manuel Richter,[2] and Levente Vitos[1,3,4]

[1]*Applied Materials Physics, Department of Materials Science and Engineering, KTH Royal Institute of Technology, SE-10044 Stockholm, Sweden*

[2]*IFW Dresden and Dresden Center for Computational Materials Science, D-01069 Dresden, Germany*

[3]*Department of Physics and Astronomy, Division of Materials Theory, Uppsala University, Box 516, SE-75120 Uppsala, Sweden*

[4]*Research Institute for Solid State Physics and Optics, Wigner Research Center for Physics, P.O. Box 49, H-1525 Budapest, Hungary*

(Received 2 March 2018; revised manuscript received 17 May 2018; published 12 June 2018)

We investigate the lattice dynamical properties of Ni, Cu, Rh, Pd, Ag, Ir, Pt, and Au in the nonequilibrium hcp structure by means of density-functional simulations, wherein spin-orbit coupling (SOC) was considered for Ir, Pt, and Au. The determined dynamical properties reveal that all eight elements possess a metastable hcp phase at zero temperature and pressure. The hcp Ni, Cu, Rh, Pd, and Au previously observed in nanostructures support this finding. We make evident that the inclusion of SOC is mandatory for an accurate description of the phonon dispersion relations and dynamical stability of hcp Pt. The underlying sensitivity of the interatomic force constants is ascribed to a SOC-induced splitting of degenerate band states accompanied by a pronounced reduction of electronic density of states at the Fermi level. To give further insight into the importance of SOC in Pt, we (i) focus on phase stability and examine a lattice transformation related to optical phonons in the hcp phase and (ii) focus on the generalized stacking fault energy (GSFE) of the fcc phase pertinent to crystal plasticity. We show that the intrinsic stable and unstable fault energies of the GSFE scale as in other common fcc metals, provided that the spin-orbit interaction is taken into account.

DOI: 10.1103/PhysRevB.97.224305

I. INTRODUCTION

Relativistic effects are responsible for a number of intriguing phenomena and physical properties in solids. Textbook examples are the yellow color of gold and the characteristic humming of transformers. Several properties in magnetic materials, such as magnetocrystalline anisotropy, the magneto-optic Faraday and Kerr effects, and the anomalous Hall effect, are due to relativistic effects and of fundamental interest and technological importance. The appropriate frame for the description of the relativistic electronic structure in solids is quantum electrodynamics, and by arguments similar to those leading to the nonrelativistic Hohenberg-Kohn theorem and Kohn-Sham scheme [1,2] a relativistic density-functional theory (DFT) for many-electron systems can be formulated, which in practice involves solving the Kohn-Sham-Dirac equation self-consistently [3–5].

The Kohn-Sham-Dirac Hamiltonian treats relativistic effects rigorously, but considering them approximately is sufficient for many solid-state applications. In scalar-relativistic approaches, the lowest-order relativistic corrections (Darwin and mass-velocity terms) are included in the Hamiltonian, but the coupling between spin and electron momentum is neglected, commonly by averaging it out [6–8]. Scalar-relativistic schemes allow for an effective approximative treatment since the solutions of the Kohn-Sham equations are spin-up and spin-down eigenstates for collinear spin magnetic moment orientations. For an adequate description of heavy elements, such as actinides, and many magnetic ground- and excited-state properties (see examples above), spin-orbit coupling (SOC) also has to be included in the Hamiltonian. In plane-wave codes, for instance, this is achieved through a second variational approach after diagonalizing the scalar-relativistic Hamiltonian [9]. Other band structure codes use a transformation of the Kohn-Sham-Dirac Hamiltonian to an effective two-component regular Hamiltonian, which includes SOC to zeroth order in the expansion [10,11]. Finally, a few codes rely on a four-component Kohn-Sham-Dirac implementation [12–15].

The importance of relativistic effects on electronic properties of atoms, molecules, and elemental solids was thoroughly studied [16–19]. Much less research in this direction has been conducted on bulk phase stability and lattice dynamical properties of elements, and among those efforts most attention has been paid to the $6p$ systems Pb, Bi, and Po. For instance, it was observed that SOC is essential for a correct representation of the phonon frequencies in the α and β phases of Po and crucial for the phononic contribution to their competing thermodynamic stability [20–22]. Díaz-Sánchez *et al.* demonstrated a significant, wave-vector-dependent softening of optical phonon frequencies along with improved agreement with experimental dispersion relations in rhombohedral Bi upon including SOC in the determination of the interatomic force constants (IFCs) [23]. A similar phonon softening effect of SOC was found for fcc Pb, whereas both scalar-relativistic and relativistic treatments reproduced Kohn anomalies in

*stesch@kth.se
†xiaoqli@kth.se

the dispersion relations, although at different wave vectors [24].

The present DFT investigation is, on the one hand, concerned with the bulk lattice dynamical properties and possible metastability of eight transition- and noble-metal elements, Ni, Cu, Rh, Pd, Ag, Ir, Pt, and Au, in a nonequilibrium hcp structure at zero temperature and pressure. Whereas none of these elements possesses a second known allotrope besides the fcc configuration in its pressure-temperature phase diagram [25,26], the driving force for this work is the expectation that a metastable phase may have different properties than its stable counterpart. In particular, there has been growing interest in nanostructures in nonequilibrium crystal structures, possibly isostructural to metastable bulk phases, due to their potentially size- or shape-enhanced mechanical, optical, electronic, magnetic, or catalytic properties. Motivated by our recent finding that the fcc structures of the hcp stable elements Sc, Ti, Co, Y, Zr, Tc, Ru, Hf, Re, and Os are metastable [27], we here address the complementary question: do the fcc stable transition and noble elements Ni, Cu, Rh, Pd, Ag, Ir, Pt, and Au possess a metastable hcp bulk phase? We make evident that the inclusion of SOC is mandatory for an accurate description of the lattice dynamics and stability of hcp Pt, unlike in its 5*d* neighbors Ir and Au.

On the other hand, we lend fundamental insight into relativistic effects on the electronic structure and force constants of hcp Pt and examine a displacive lattice transformation related to zone-centered optical phonons in the hcp structure in order to show the impact of SOC on the bulk phase stability of Pt. We also analyze the generalized stacking fault (GSF) of fcc Pt pertinent to the atomistic theory of crystal plasticity and demonstrate the importance of SOC for the intrinsic stable and unstable fault energies of the GSF.

The remainder of paper is organized as follows. We begin by describing methodology and computational details in Sec. II. In Sec. III we briefly present and discuss the lattice dynamical properties of hcp Ni, Cu, Rh, Pd, Ag, Ir, Pt, and Au. Then we elaborate on the effect of SOC on the IFCs and phonon dispersions in hcp Pt, on the displacive lattice transformation in Pt, and on the GSF energy (GSFE) in fcc Pt. Section IV concludes with a summary, highlights the significance of this study, and presents a brief outlook.

II. METHODOLOGICAL AND COMPUTATIONAL DETAILS

A. Lattice stability

In terms of the phonon frequency ν, the criterion for dynamical lattice stability in the harmonic approximation reads [28]

$$\nu^2(\boldsymbol{q},s) > 0 \tag{1}$$

for all wave vectors $\boldsymbol{q}$ in the first Brillouin zone, polarizations, and phonon branches s. Elastic instabilities connected to acoustic long-wavelength phonon modes are scrutinized separately, as sampling the force constants for wave vectors close to the Γ point is computationally not feasible in the present phonon calculator. Elastic stability in the absence of external forces requires a positive-definite strain energy (in standard Voigt notation) [29]:

$$E(\boldsymbol{\epsilon}) - E_{\rm hcp} = \frac{V_{\rm hcp}}{2} \sum_{\alpha,\beta=1}^{6} C_{\alpha\beta}\epsilon_\alpha\epsilon_\beta > 0 \tag{2}$$

for any small strain matrix $\boldsymbol{\epsilon} \neq \boldsymbol{0}$. $E_{\rm hcp}$ denotes the total energy of an hcp structure in equilibrium with the corresponding atomic volume $V_{\rm hcp}$. There are five independent elastic constants $C_{\alpha\beta}$ for hexagonal crystal symmetry, C_{11}, C_{12}, C_{13}, C_{33}, and C_{44}, and in addition the relation $C_{66} = (C_{11} - C_{12})/2$ holds. The elastic stability can be judged from the following Born criteria [29]:

$$C_{44} > 0, \tag{3a}$$

$$C_{11} - |C_{12}| > 0, \tag{3b}$$

$$(C_{11} + C_{12})C_{33} - 2C_{13}^2 > 0. \tag{3c}$$

To compute the elastic constants, we monitored and fitted the energy vs strain relation [Eq. (2)] for the strain tensors detailed by Fast *et al.* [30]. The largest employed strain component was 0.02.

B. Generalized stacking fault

The GSFE specifies the minimum-energy pathway of creating a planar crystal fault with a specific degree of lattice shearing [31]. The GSFE curve was obtained for the fcc $\{111\}\langle 11\bar{2}\rangle$ family of slip systems by rigidly shearing two parts of the crystal along the displacement vector $\boldsymbol{u} \| \boldsymbol{b}_p$ for two different pathways. The partial Burgers vector equals $\boldsymbol{b}_p = a_{\rm fcc}/6\langle 11\bar{2}\rangle$, with $a_{\rm fcc}$ being the fcc equilibrium lattice parameter. The fault energy $\gamma(\boldsymbol{u})$ is normalized by the area A per atom in a $\{111\}$ close-packed layer,

$$\gamma(\boldsymbol{u}) = \frac{E_{\rm sheared}(\boldsymbol{u}) - E_{\rm fcc}}{A}, \tag{4}$$

where $E_{\rm sheared}$ and $E_{\rm fcc}$ are the energies of the sheared structure and the fault-free fcc structure, respectively. The first considered pathway transforms the fcc lattice into an fcc lattice with an intrinsic stacking fault (ISF) with corresponding energy $\gamma_{\rm ISF} \equiv \gamma(\boldsymbol{b}_p)$, whereas the second pathway transforms the fcc lattice with ISF into an fcc lattice with an extrinsic stacking fault (ESF) with corresponding energy $\gamma_{\rm ESF} \equiv \gamma(2\boldsymbol{b}_p)$; see Fig. 1 for a sketch. It should be noted that these paths involve shearing on two successive close-packed planes. The energy barriers occurring on the first pathway and second pathway are referred to as the unstable stacking fault (USF) and unstable twinning fault (UTF) with energies $\gamma_{\rm USF}$ and $\gamma_{\rm UTF}$, respectively [32].

C. Total energy and phonon calculations

We employed the Vienna Ab initio Simulation Package (VASP) [33–35] and the all-electron full-potential local orbital (FPLO) scheme [12]. FPLO calculations with the scalar-relativistic approximation are denoted by FPLO-SR, whereas relativistic FPLO calculations using the four-component Kohn-Sham-Dirac implementation [13] are denoted by FPLO-FR. A detailed account of the numerical parameters for total energy and phonon calculations is given in the Supplemental Material [36], which includes Refs. [37–46].

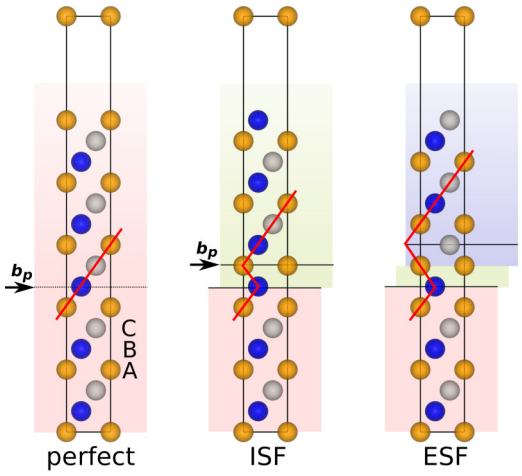

FIG. 1. Illustration of the crystal configuration at different stages of the GSF (from left to right, perfect fcc lattice, lattice with ISF, and lattice with ESF) and repeated slab geometry for calculating the GSFE surface. The letters A, B, and C, as well the corresponding color code, denote the stacking sequence, and the arrows indicate the slip planes with slip vector $\boldsymbol{b}_p$.

III. RESULTS AND DISCUSSION

A. Structure and metastability of hcp states

The equilibrium geometries of Ni, Cu, Rh, Pd, Ag, Ir, Pt, and Au in the hcp structure $[a_{\rm hcp},(c/a)_{\rm hcp}]$ as computed with VASP are listed in Table I. All elements apart from the isoelectronic Rh and Ir possess an axial distortion larger than the "ideal" value $\sqrt{8/3} \approx 1.633$. Pt seems to stick out as its ratio of 1.710 is significantly larger than those of the other considered elements. According to a previous DFT investigation and canonical band theory treatment for the *entire* transition-metal family [47], the $(c/a)_{\rm hcp}$ ratio varies canonically as any of the three series is traversed, which mainly originates from the one-electron d-band energy. The deviation of $(c/a)_{\rm hcp}$ from $\sqrt{8/3}$ was found to peak for the elements of the ninth group, Ni, Pd, and Pt, in agreement with the present results. It should be pointed out that Ducastelle and Cyrot-Lackmann already employed the fourth-order moment theory of the site-resolved electronic density of states (DOS) to qualitatively show that a slight decrease (increase) in c/a from $\sqrt{8/3}$ would stabilize the hcp structure in the hcp (fcc) stability range [48].

As is evident from the calculated elastic constants listed in Table I, the Born criteria (3c), and the computed phonon dispersion relations and DOSs shown in the Supplemental Material [36], the hcp structures of Ni, Cu, Rh, Pd, Ag, Ir, Pt, and Au are dynamically stable. As their hcp total energies lie above those of their fcc phases (Table I), these eight structures are predicted to be metastable bulk phases at zero temperature and pressure. It should be noted that the metastablity of hcp Au was reported before [49]. In Table I we also list the elastic Debye temperatures $\theta_{\rm D}$ derived from the mean sound velocity of single-crystalline solids [50].

There is experimental evidence for hcp nanocrystalline structures in support of several of these metastable bulk phases: Ni in hcp structure was produced via various preparation routes, for instance, in pulsed laser deposited films [51], in thin-film heteroepitaxial growth [52], and during low-temperature annealing in nanograined thin films [53]. Nanoparticles of hcp Rh were recently stabilized by means of electron-irradiation-induced decomposition or chemical syntheses [54], and up to 16-monolayer-thick hcp Au sheets could be synthesized on graphene oxide [55]. Observations of hcp Pd and Cu island growth on a tungsten substrate were reported by Wormeester *et al.* [56,57]. To the best of our knowledge, the hcp structure has not been experimentally verified yet for the other elements (Ag, Ir, and Pt).

B. Spin-orbit-coupling-induced metastability of hcp Pt

To start with, we investigate the influence of relativistic effects beyond the scalar-relativistic approximation on the lattice parameters of hcp and fcc Pt (see Table II). Obviously, relativity causes a small expansion of $a_{\rm hcp}$ (0.3% VASP, 0.7% FPLO) accompanied by a reduction of the c/a ratio (each 0.7%), leading to an increased atomic volume (0.2% VASP, 1.4% FPLO). Changes of similar magnitude are found for the fcc equilibrium lattice parameter $a_{\rm fcc}$, although the effect is much more pronounced in FPLO, and for the hcp-fcc energy difference (see Table II). With respect to the experimentally determined lattice parameter of fcc Pt at room temperature, 3.923 Å [58], the inclusion of SOC improves the agreement of the theoretical results.

Second, in order to measure the impact of SOC on the interatomic forces, we computed the phonon dispersion relations of hcp Pt with and without invoking SOC. These calculations were done for fixed geometry (we chose the scalar-relativistic geometry) in order to disentangle any effect arising from the

TABLE I. Structural parameters, energy difference per atom $\Delta E_{\rm hcp} \equiv E_{\rm hcp} - E_{\rm fcc}$, elastic constants, and elastic Debye temperature for the metastable hcp structures of the investigated fcc stable elements. SOC was invoked for Ir, Pt, and Au.

Element	$a_{\rm hcp}$ (Å)	$(c/a)_{\rm hcp}$	$\Delta E_{\rm hcp}$ (meV)	C_{11} (GPa)	C_{12} (GPa)	C_{33} (GPa)	C_{44} (GPa)	C_{13} (GPa)	$\theta_{\rm D}$ (K)
Ni	2.485	1.642	24	340	125	337	60	124	461
Cu	2.568	1.638	8	225	99	246	42	88	365
Rh	2.723	1.613	37	432	152	431	75	176	406
Pd	2.763	1.683	33	247	131	250	22	125	250
Ag	2.929	1.641	3	143	71	154	21	59	221
Ir	2.710	1.625	67	678	237	666	111	267	368
Pt	2.721	1.710	66	471	233	411	27	219	228
Au	2.836	1.673	6	257	185	264	26	162	174

TABLE II. Structural parameters of fcc and hcp Pt and the energy difference $\Delta E_{\rm hcp} \equiv E_{\rm hcp} - E_{\rm fcc}$ from VASP with and without SOC, as well as FPLO in the scalar-relativistic and relativistic modes. The energy difference $\Delta E_{\rm fco} \equiv E_{\rm fco} - E_{\rm fcc}$ discussed in Sec. III C is also listed. The lattice parameters are in angstroms and the energies are in meV per atom.

	Structure			Energy	
	fcc	hcp		hcp	fco
Method	$a_{\rm fcc}$	$a_{\rm hcp}$	$(c/a)_{\rm hcp}$	$\Delta E_{\rm hcp}$	$\Delta E_{\rm fco}$
VASP	3.897	2.713	1.722	65	16
VASP+SOC	3.899	2.721	1.710	66	40
FPLO-SR	3.881	2.704	1.718	74	18
FPLO-FR	3.906	2.723	1.706	69	39

geometry change accompanying SOC (see Fig. 2). Accordingly, scalar-relativistic hcp Pt is predicted to be unstable as imaginary optical modes on the transverse phonon branches near the $\Gamma(0,0,0)$ and $A(0,0,1/2)$ high-symmetry points occur. The SOC clearly removes all imaginary optical modes and hardens the acoustic modes along several high-symmetry directions, in particular Γ-K and Γ-M, but leads to virtually no change in the maximum phonon frequency. The impact of the geometry change accompanying SOC is minor as the comparison of Fig. 2 with Fig. 2 from the Supplemental Material [36] makes evident; that is, the phonon bandwidth decreases by ∼0.1 THz, but there is obviously no change in the band topology.

The effect of SOC on the phonon dispersion relations calls for an analysis of the 3×3 IFC matrix $\Phi_{\alpha\beta}(\kappa,\kappa')$ for a pair of atoms κ and κ', where α and β denote the Cartesian coordinate indices (for $\kappa = \kappa'$, $\Phi_{\alpha\beta}$ is referred to as the on-site term). For the present purpose it is sufficient to mainly focus on the trace denoted by Tr Φ. Table III lists the traces with and without considering SOC, Tr $\Phi^{\rm SOC}$ and Tr Φ, respectively, as well as their difference, $\Delta{\rm Tr}\,\Phi = {\rm Tr}\,\Phi^{\rm SOC} - {\rm Tr}\,\Phi$, for those shells of atoms neighboring an arbitrary reference atom, for

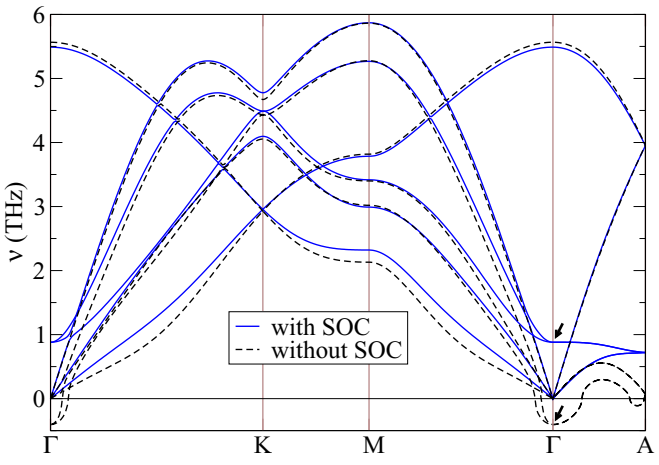

FIG. 2. Effect of SOC on the phonon dispersion relations for hcp Pt employing the scalar-relativistic geometry (see Table II). $-|\nu|$ is plotted when $\nu^2 < 0$. The arrows indicate the two optical normal modes at Γ, whose polarization vectors lie in the (0001) plane.

TABLE III. The traces of the IFC matrix (eV/Å^2) with (Tr $\Phi^{\rm SOC}$) and without (Tr Φ) the inclusion of SOC, as well as their difference ($\Delta{\rm Tr}\,\Phi = {\rm Tr}\,\Phi^{\rm SOC} - {\rm Tr}\,\Phi$), for different shells of atoms for hcp Pt employing the scalar-relativistic geometry. The shell coordinate triplets (klm) give the location of one site per shell (the number of equivalent sites is in square brackets) relative to an arbitrary reference atom in terms of the conventional hcp basis vectors ($k\boldsymbol{a}_1 = ka_{\rm hcp}\boldsymbol{e}_x$, $l\boldsymbol{a}_2 = la_{\rm hcp}/2\boldsymbol{e}_x + l\sqrt{3}/2a_{\rm hcp}\boldsymbol{e}_y$, $m\boldsymbol{a}_3 = mc_{\rm hcp}\boldsymbol{e}_z$). The distance is in angstroms, and only shells for which $|\Delta{\rm Tr}\,\Phi| \geqslant 0.03$ eV/Å^2 are listed.

Shell	Distance	Tr $\Phi^{\rm SOC}$	Tr Φ	ΔTr Φ
(000) [1]	0	32.494	31.745	0.749
(100) [6]	2.713	−3.299	−3.269	−0.030
(001) [2]	4.671	−0.244	−0.182	−0.062
(210) [6]	4.699	−0.304	−0.340	−0.036
(200) [6]	5.426	0.747	0.860	−0.113
$(\frac{4}{3}\frac{8}{3}\frac{1}{2})$ [6]	6.687	−0.121	−0.066	−0.055
(002) [2]	9.341	−0.211	−0.330	0.119

which $|\Delta{\rm Tr}\,\Phi| \geqslant 0.03$ eV/Å^2. The force-constant matrices were analyzed for the scalar-relativistic geometry. The notation of a shell (klm) is given in the caption of Table III.

As is evident, the on-site force constants (000) are the largest; Tr Φ and Tr $\Phi^{\rm SOC}$ rapidly decay with distance due to valance electron screening, and both traces exhibit an oscillatory pattern with distance. In terms of absolute values, the SOC clearly has the largest impact on the on-site term, whose increase of 0.749 eV/Å^2 arises almost entirely from the in-plane contributions of $\Delta\Phi_{xx} = \Delta\Phi_{yy} = 0.383$ eV/Å^2. Surprisingly, SOC has significantly smaller effects on the nearest-neighbor shell (100) and the next-nearest-neighbor shell $(\frac{1}{3}\frac{2}{3}\frac{1}{2})$ (not listed in Table III since $|\Delta{\rm Tr}\,\Phi| < 0.03$ eV/Å^2) than the more distant shells (200) and (002) with distance equal to $2a_{\rm hcp}$ and $2c_{\rm hcp}$, respectively. Thus, the perturbation of the force constants due to SOC extends to at least two lattice spacings. Larger supercell calculations would be required to determine the full range.

SOC affects the IFCs since it influences the underlying electronic structure and may thus alter the screening of forces on the ion cores. In an hcp structure (point group D^4_{6h}), the scalar d-wave functions transform according to the irreducible representations A_{1g}, E_{1g}, and E_{2g}. Figure 3(a) shows the $5d$-band-dominated total electronic DOS of hcp Pt in the scalar-relativistic and relativistic modes computed with FPLO. In the scalar-relativistic case, there is a pronounced peak 0.12 eV below the Fermi level, which arises mainly from the E_{1g} states. This peak is due to a flat band with bandwidth ≈1 eV [see Fig. 3(b)], in which the weighted E_{1g} contribution to the band states is also shown. The SOC splits degenerate band states and leads to new singular features in the DOS [see Figs. 3(a) and 3(c)]. The spin-orbit splitting at the center of the Brillouin zone amounts to approximately 0.8 eV for the highest occupied band. The relativistic treatment narrows the peak at the Fermi level primarily by band splitting, thereby significantly lowering the DOS at the Fermi energy. The relativistic effects also alter the topology of the Fermi surface shown in the Supplemental

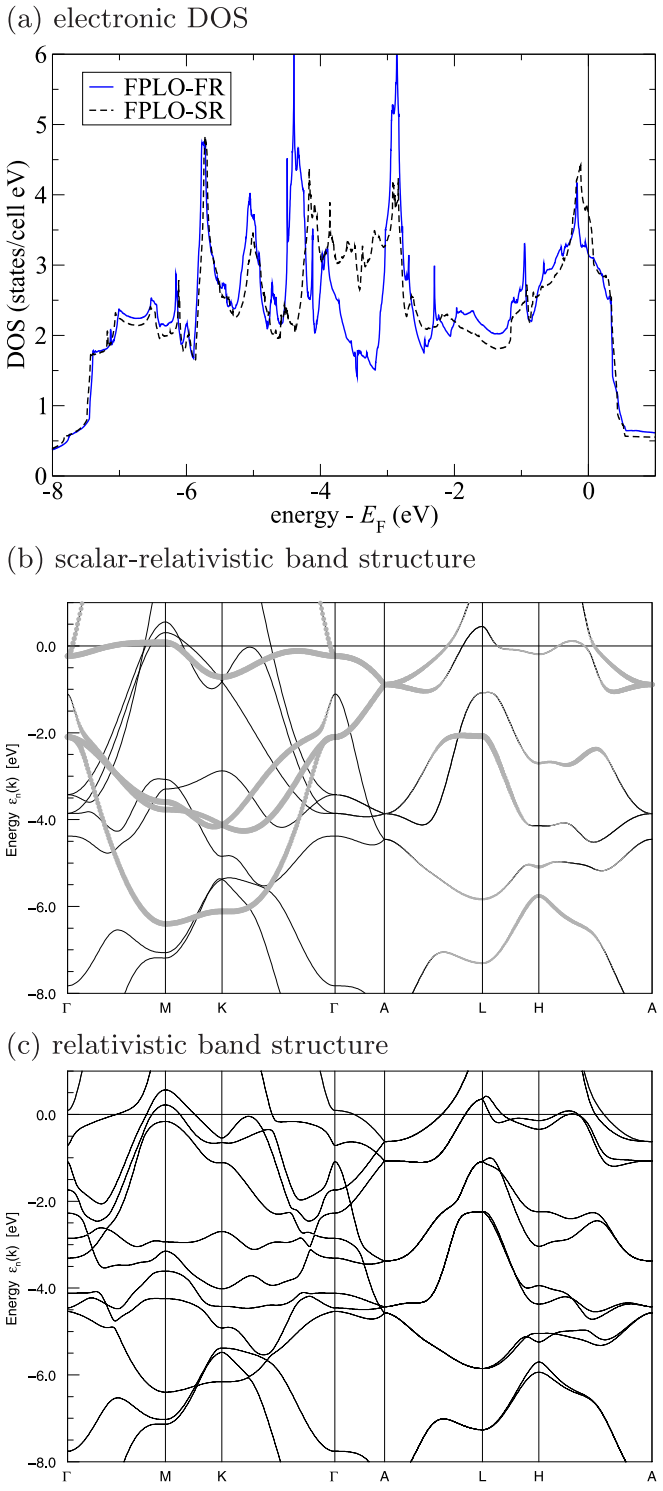

FIG. 3. The electronic structure of hcp Pt. (a) Total electronic DOS in the scalar-relativistic and relativistic modes with FPLO. (b) FPLO-SR band structure and the E_{1g} band weights represented by gray ribbons. (c) FPLO-FR band structure. The equilibrium geometries were employed (see Table II).

Material [36] by removing hole pockets centered at M and lying on M-L and splitting a funnel-shaped hole surface into two disconnected ones. We partially attribute the strong impact of SOC on the IFCs to this reduction of states at the Fermi level, which in turn reduces the screening [59]. Given the complexity of the Fermi surface of Pt (as opposed to that of a simple free-electron metal), we expect that the electronic structure origin involves more intricate details, for instance, a dependence of the electronic screening on the size and shape of the Fermi surface [60], but addressing these aspects is beyond the scope of this work.

It is instructive to contrast these results for Pt with the impact of SOC on the phonon dispersion relations for Ir and Au, which, as neighbors in the periodic table, have comparable spin-orbit interaction strengths. From the corresponding phonon dispersion relations shown in the Supplemental Material [36], it is clear that SOC leads to a minor change in the dispersion relations (maximum $|\Delta\nu| = 0.07$ THz) without notably affecting the phonon band topology. The flat band of predominantly E_{1g} character that was suggested to play an important role in hcp Pt can be ruled out to be decisive. In Au, the $5d$ bands are completely filled, and the Fermi surface is determined by free-electron-like $6s$ states. In Ir, which has one electron less than in Pt, this band is almost empty.

The SOC-induced metastability of hcp Pt is a surprising result since SOC commonly does not affect structural stability. To lend further insight into the impact of relativistic effects on structural stability in Pt and what further distinguishes it from the other elements, we next examine a lattice transformation.

C. The hcp to fco lattice transformation in Pt

The investigated displacive lattice transformation brings the hcp structure into the face-centered-orthorhombic (fco) structure. The initial part of this transformation is related to the zone-centered, optical phonons of hcp Pt with the displacement vector parallel to the $[1\bar{1}00]$ direction, for brevity denoted by $O_{[1\bar{1}00]}[\Gamma]$. An analysis of the phonon normal modes at the Γ point revealed that the polarization vectors of two optical, energetically degenerate normal modes lie in the (0001) plane, but not parallel to the $[1\bar{1}00]$ direction. Thus, $O_{[1\bar{1}00]}[\Gamma]$ does not correspond to a single excited optical normal mode, but rather to a superposition of both optical normal modes.

The hcp to fco lattice transformation was modeled as a "frozen" phonon mode. It is governed by a displacement of the two types of close-packed (0001) planes in opposite directions, i.e., alternating in $[1\bar{1}00]$ and $[\bar{1}100]$ for all A and all B layers, respectively, where $ABAB$ denotes the hcp stacking sequence; see Fig. 4(a) for a sketch. In order to describe this transformation, we use the displacement variable δ, which is linear in the displacement strain and defined to be 0 and 1 at the initial state [hcp structure, space group $P6_3/mmc$ (194)] and the final state [fco structure, space group $Fmmm$ (69)], respectively. The transformation was modeled by the orthorhombic space group $Cmcm$ (63), which is a subgroup of both the initial and final structures. During the displacement we assumed that the cell volume is constant; that is, neither the interplanar distances between adjacent (0001) planes nor their in-plane dimensions were allowed to change. Due to these constraints, the lattice parameters of the fco structure, a_{fco}, b_{fco}, and c_{fco} as defined in Fig. 4(a), are related to the hcp lattice parameters through $a_{\mathrm{fco}} = a_{\mathrm{hcp}}$, $b_{\mathrm{fco}} = \sqrt{3}a_{\mathrm{hcp}}$, and $c_{\mathrm{fco}} = c_{\mathrm{hcp}}$. A brief comment on the effect of relaxation is provided in the Supplemental Material [36].

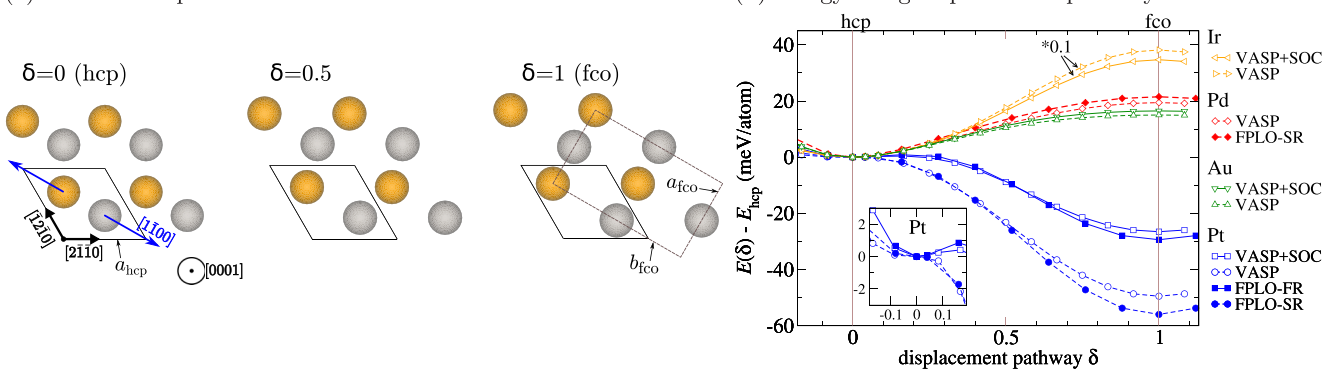

FIG. 4. (a) Sketch of the hcp to fco transformation at the initial ($\delta = 0$), intermediate ($\delta = 0.5$), and final ($\delta = 1$) stages by means of displacing the two types of hcp (0001) planes alternating in the $[1\bar{1}00]$ and $[\bar{1}100]$ directions. Atoms residing in the two planes are colored differently. The basal plane of the fco structure with lattice parameters a_{fco} and b_{fco} is indicated at $\delta = 1$. c_{fco} (not depicted) measures the height of the fco unit cell perpendicular to the image's plane. (b) Total energy difference $E(\delta) - E_{hcp}$ for the transformation of Pt in comparison to Pd, Ir (energies rescaled by a factor of 0.1), and Au. The inset shows the energies of Pt for small δ.

In the scalar-relativistic approximation, the phonon frequencies for both these optical normal modes are imaginary (Fig. 2), indicating that hcp Pt would spontaneously transform into a different structure with lower energy. This is confirmed by the scalar-relativistic total energies along the lattice transformation [see Fig. 4(b)]. As δ is increased from 0 to 1, the total energy decreases until it reaches a symmetry-dictated minimum in energy that coincides with the fco structure. From the VASP (FPLO-SR) calculations, we find that the total energy of the fco structure lies approximately 49 meV (56 meV) lower in energy than that of the hcp state [see Fig. 4(b)]. In contrast, the VASP+SOC and FPLO-FR total energy curves exhibit a shallow minimum at $\delta = 0$, which is in line with the real phonon frequencies for the optical normal modes at Γ (Fig. 2 from the Supplemental Material [36]), and a local maximum at $\delta \approx 0.16$. This supports the scenario that the SOC-induced splitting in the electronic band structure described in the previous section stabilizes the hcp band energy against a Jahn-Teller-like band distortion, which lifts the twofold-degenerate E_{1g} representation of the scalar d-wave functions. Similar to the scalar-relativistic results, the VASP+SOC and FPLO-FR energy curves exhibit a minimum at $\delta = 1$. SOC reduces the fco-hcp energy difference by 23 and 26 meV in the VASP+SOC and FPLO-FR calculations, respectively. Thus, although all phonon frequencies in relativistic hcp Pt are predicted to be real at 0 K, the hcp structure is only barely stable due to the shallow energy barrier along the hcp to fco transformation path, which is likely to be overcome by thermal lattice vibrations at rather low temperatures.

It is instructive to investigate the hcp to fco transformation path for a few other elements, and we chose isoelectronic Pd, as well as Ir and Au. As is evident from the total energies shown in Fig. 4(b), the relative stability of the hcp and fco structures of Pd, Ir, and Au is inverted, irrespective of SOC, and $E(\delta)$ is a monotonically increasing function of δ ($0 \leqslant \delta \leqslant 1$). The SOC decreases $E_{fco} - E_{hcp}$ of Ir by 35 meV. The total energies of the other investigated elements, Ni, Cu, Rh, and Ag, are also found to order as $E_{fcc} < E_{hcp} < E_{fco}$. Thus, Pt is an exception since $E_{fcc} < E_{fco} < E_{hcp}$. It should be stressed that this exceptional order is not a result of spin-orbit effects as the same order is found in the scalar-relativistic treatment of Pt.

D. GSFE of Pt

The results in the previous sections showed that SOC insignificantly alters the relative energetic stability of the close-packed fcc and hcp structures of Pt, whereas a pronounced effect on the total energy difference was demonstrated for more open structures on the hcp to fco deformation path. Here, we focus on the GSF of fcc Pt, which may be viewed as a local perturbation of the close-packed arrangement near fault planes, depending on the position on the fault pathway, and investigate the impact of SOC on the GSFE curve. Of special significance are the extrema on the GSFE curve, combinations of which were hypothesized to govern the activation of competing plastic deformation modes in the atomistic theory of plasticity in fcc crystals [32,61–63]. In this context it was reported [64] that the fault energies in Pt do not scale as in common fcc transition, noble, and nearly-free-electron metals. This point is addressed further below.

The GSFE curves $\gamma(u)$ computed with VASP are shown in Fig. 5(a) as a function of the magnitude of the displacement vector $u = |\boldsymbol{u}|$. The most notable effect of SOC is a reduction of both γ_{ISF} and γ_{ESF} by approximately 20 mJ/m^2, or 6% (a rule of thumb states $\gamma_{ISF} \simeq \gamma_{ESF}$), and an increase of the barriers $\gamma_{USF} - \gamma_{ISF}$ and $\gamma_{UTF} - \gamma_{ISF}$. The position of the USF at $u(\gamma_{USF})/b_p \approx 0.7$ is located relatively far from the midpoint of the first pathway at $0.5b_p$. The position of this saddle point, as well as that of the UTF at $u(\gamma_{UTF})/b_p \approx 1.5$, is fairly stable against invoking SOC. It is also evident that the interlayer relaxation on the fault energy curve is generally significant, in particular for the saddle-point energies.

Table IV summarizes the present intrinsic stable and unstable fault energies along with available DFT data, which neglected SOC throughout, and the experimentally determined γ_{ISF}. It should be highlighted that in contrast to Refs. [64,65] but in accordance with Refs. [66,67], we report a pronounced barrier height $\gamma_{USF} - \gamma_{ISF}$ and a significantly larger barrier $\gamma_{UTF} - \gamma_{ISF}$ compared to the theoretical data from Ref. [64].

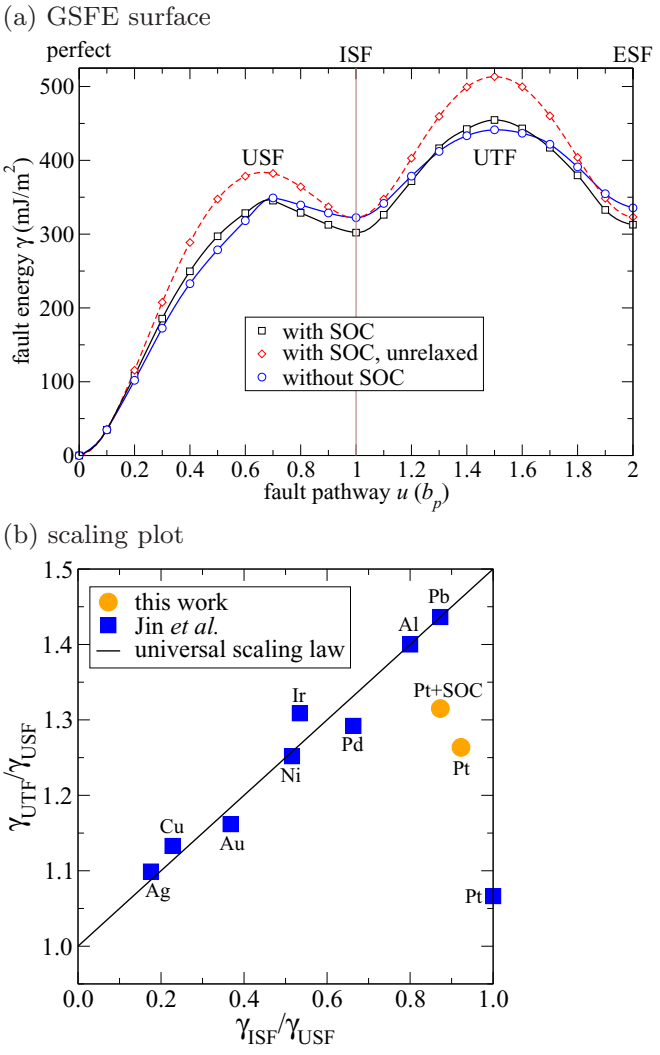

FIG. 5. (a) GSFE surface γ of Pt with fault pathway $u = |\boldsymbol{u}|$ given in fractions of the magnitude of the partial Burgers vector $b_p = |\boldsymbol{b}_p|$. (b) Scaling plot for stable and unstable fault energies of the GSFE with our values for Pt computed with and without invoking SOC, DFT data taken from Jin *et al.* (neglecting SOC) [64], and the scaling law (5) suggested in Ref. [64].

The experimental estimate for γ_{ISF} amounts to 322 mJ/m^2 at 298 K [68], but as the corresponding temperature coefficient $d\gamma_{\mathrm{ISF}}/dT \approx -0.08$ (mJ/m^2)/K is negative [68], the low-temperature experimental value is larger by approximately 24 mJ/m^2 assuming a linear extrapolation with temperature. Keeping in mind that the accuracy of experimental ISF energies in fcc elements was estimated to be approximately 20 % [69], we conclude good agreement with the presently derived γ_{ISF}.

The obtained data allow examining a previously suggested universal scaling law [64],

$$\frac{\gamma_{\mathrm{UTF}}}{\gamma_{\mathrm{USF}}} \simeq \frac{1}{2}\frac{\gamma_{\mathrm{ISF}}}{\gamma_{\mathrm{USF}}} + 1, \tag{5}$$

which would be fulfilled provided that the fault energy barrier for the sequentially faulted lattice (i.e., along the second pathway) does not strongly interact with the preexisting ISF. Jin *et al.* [64] found that Eq. (5) does not apply to scalar-relativistic

TABLE IV. Relaxed stable and unstable fault energies (mJ/m^2) on the GSFE surface of fcc Pt evaluated with and without SOC. Other DFT (neglecting SOC) and available experimental literature data are tabulated for comparison.

Approach	γ_{USF}	γ_{ISF}	γ_{UTF}	γ_{ESF}
Theory				
This work, with SOC	346	302	455	313
This work, without SOC	349	322	441	336
Ref. [64][a]	286	286	305	284
Ref. [67][b,c]	339	324	486	
Ref. [65][b]	258	254		
Ref. [66][b]	311	282		
Experiment				
Ref. [68] (298 K)		322		

[a] VASP, functional not published.
[b] VASP, PBE [37].
[c] Experimental lattice parameter used.

Pt owing to a strongly reduced γ_{UTF}; see the scaling plot in Fig. 5(b). In contrast, we find that scalar-relativistic Pt obeys the scaling relation more strictly, and SOC brings it significantly closer to the universal line equation (5), meaning that the stable and unstable fault energies in Pt do indeed scale as in other common fcc metals. Nevertheless, Pt is the element that lies farthest from the universal scaling law [Fig. 5(b)]. This supports the conclusion from Ref. [64], although in attenuated form, that the coupling between the transition state for nucleation of the two-layer nanotwin and the preexisting intrinsic stacking fault extends to several adjacent planes. Possible reasons for the disagreement between this work and Jin *et al.* for scalar-relativistic Pt are ascribed to differences in numerical treatment (plane-wave cutoff, k-point integration scheme, size of supercell, and thickness of vacuum), the procedure of mapping out the GSFE, and the exchange-correlation functional, all of which may affect the fault energies.

IV. SUMMARY AND CONCLUSIONS

We presented a DFT investigation of lattice dynamical properties of Ni, Cu, Rh, Pd, Ag, Ir, Pt, and Au in the hcp structure, wherein SOC was considered for Ir, Pt, and Au. All eight investigated elements are dynamically stable in the hcp structure and thus presumably metastable bulk phases at zero temperature and pressure. The existing experimental evidence for hcp Ni, Cu, Rh, Pd, and Au in nanocrystalline structures is supports these isostructural metastable bulk phases. The metastability of the other hcp phases has not been experimentally observed yet and thus is predicted here.

This investigation complements our previous density-functional study [27], which suggested that the fcc structures of the hcp stable elements Sc, Ti, Co, Y, Zr, Tc, Ru, Hf, Re, and Os are metastable at 0 K. Taking both studies together, the theoretical picture that has now evolved is that all transition and noble-metal elements stable in the hcp (fcc) structure are predicted to possess a metastable bulk fcc (hcp) phase.

Unlike hcp Ir and Au, the inclusion of SOC was shown to be mandatory for an accurate description of the phonon dispersion relations and dynamical stability in hcp Pt. A scalar-relativistic

treatment of hcp Pt was found to lead to imaginary optical modes. We showed that the SOC most notably perturbs the on-site IFCs and the perturbation extends to no less than two lattice spacings. The electronic structure reason for this change in the screening of forces was ascribed, at least in part, to a pronounced reduction of electronic DOS at the Fermi level due to a SOC-induced splitting of degenerate band states of predominantly E_{1g} character.

To further examine the role of SOC in Pt, on the one hand, we focused on the hcp to fco lattice transformation. We found that Pt is the only investigated element for which $E_{\mathrm{fco}} < E_{\mathrm{hcp}}$. This phase transformation would spontaneously occur in scalar-relativistic hcp Pt due to an unstable Γ-centered optical phonon mode, but it is suppressed in relativistic Pt due to the formation of a local maximum on the displacement pathway, in agreement with the computed phonon spectra. On the other hand, SOC causes significant changes in the stacking fault energies and fault energy barriers of the GSFE curve of fcc Pt. It should be stressed that the present intrinsic stable and unstable fault energies in Pt were found to scale as in other common fcc metals according to a previously suggested universal scaling law [64], provided that the effect of SOC on the total energy is considered. To summarize, relativistic effects in Pt are too significant to be neglected in an adequate description of its electronic structure, phase stability, and dynamical and micromechanical properties.

This work raises several further questions, for instance, if pairs of stable and metastable close-packed polytypes do also exist in substitutionally disordered close-packed alloys. This question is intimately related to the ongoing search for the thermodynamic ground state and polymorphism in some high-entropy alloys [70,71], as well as the production of dual-phase (fcc and hcp) high-entropy alloys [72]. On the other hand, polytypism is known to occur in a variety of inorganic solids, and one might wonder if polytypes with extended stacking sequences (i.e., longer periodicity) do exist in transition and noble elements and what their dynamical properties are.

Moreover, the present findings are relevant in the context of computing the temperature dependence of the intrinsic or extrinsic stacking fault energies through the axial Ising model [73], where the dynamical stability of the involved closed-packed polytypes is a mandatory requirement for determining vibrational free energies. Since ideal (i.e., laterally unbound) ISFs can be viewed as a two-layer hcp nucleus in the fcc matrix (see Fig. 1), one may also extend this investigation to the lattice dynamical properties of an ISF embedded in the fcc host, with a particular focus on interfacial effects.

ACKNOWLEDGMENTS

Financial support from the Swedish Research Council, the Carl Tryggers Foundation for Scientific Research, the Swedish Foundation for Strategic Research, the Swedish Foundation for International Cooperation in Research and Higher Education, Sweden's Innovation Agency (VINNOVA Grant No. 2014-03374), the Swedish Energy Agency, and the Hungarian Scientific Research Fund (OTKA 109570) is gratefully acknowledged. The Swedish National Infrastructure for Computing at the National Supercomputer Centers in Linköping, Umeå, and Stockholm is acknowledged for providing computational facilities.

[1] P. Hohenberg and W. Kohn, Inhomogeneous electron gas, Phys. Rev. **136**, B864 (1964).

[2] W. Kohn and L. J. Sham, Self-consistent equations including exchange and correlation effects, Phys. Rev. **140**, A1133 (1965).

[3] A. K. Rajagopal and J. Callaway, Inhomogeneous electron gas, Phys. Rev. B **7**, 1912 (1973).

[4] R. M. Dreizler and E. K. U. Gross, *Density Functional Theory: An Approach to the Quantum Many-Body Problem* (Springer, Berlin, 1990).

[5] H. Eschrig, *The Fundamentals of Density Functional Theory* (Edition am Gutenbergplatz Leipzig, Leipzig, 2003).

[6] D. D. Koelling and B. N. Harmon, A technique for realistic spin-polarised calculations, J. Phys. C **10**, 3107 (1977).

[7] T. Takeda, The scalar relativistic approximation, Z. Phys. B **32**, 43 (1978).

[8] H. Gollisch and L. Fritsche, Relativistic one-particle equation for electron states of heavy metals, Phys. Status Solidi B **86**, 145 (1978).

[9] A. H. MacDonald, W. E. Picket, and D. D. Koelling, A linearised relativistic augmented-plane-wave method utilising approximate pure spin basis functions, J. Phys. C **13**, 2675 (1980).

[10] C. Chang, M. Pelissier, and P. Durand, Regular two-component Pauli-like effective Hamiltonians in Dirac theory, Phys. Scr. **34**, 394 (1986).

[11] E. van Lenthe, E. J. Baerends, and J. G. Snijders, Relativistic regular two-component Hamiltonians, J. Chem. Phys. **99**, 4597 (1993).

[12] K. Koepernik and H. Eschrig, Full-potential nonorthogonal local-orbital minimum-basis band-structure scheme, Phys. Rev. B **59**, 1743 (1999); FPLO, http://www.fplo.de.

[13] H. Eschrig, M. Richter, and I. Opahle, Relativistic solid state calculations, in *Relativistic Electronic Structure Theory, Part 2: Applications*, edited by P. Schwerdtfeger (Elsevier, Amsterdam, 2004), Chap. 12, pp. 723–776.

[14] H. Ebert, A spin polarized relativistic Korringa-Kohn-Rostoker (SPR-KKR) code for calculating solid state properties, version 7.7, http://ebert.cup.uni-muenchen.de/.

[15] H. Ebert, Fully relativistic band structure calculations for magnetic solids: Formalism and application, in *Electronic Structure and Physical Properties of Solids*, edited by H. Dreysse, Lecture Notes in Physics (Springer, Berlin, 2000), Vol. 535, pp. 191–264.

[16] *Relativistic Effects in Atoms, Molecules, and Solids*, edited by G. Malli, Nato Science Series B Vol. 81 (Springer, New York, 1983).

[17] P. Pyykkö, *Relativistic Theory of Atoms and Molecules II: A Bibliography, 1986–1992*, Lecture Notes in Chemistry Vol. 60 (Springer, Berlin, 1993).

[18] P. Pyykkö, *Relativistic Theory of Atoms and Molecules III: A Bibliography, 1993–1999*, Lecture Notes in Chemistry Vol. 76 (Springer, Berlin, 2000).

[19] A. Östlin and L. Vitos, First-principles calculation of the structural stability of 6*d* transition metals, Phys. Rev. B **84**, 113104 (2011).

[20] B. I. Min, J. H. Shim, M. S. Park, K. Kim, S. K. Kwon, and S. J. Youn, Origin of the stabilized simple-cubic structure in polonium: Spin-orbit interaction versus Peierls instability, Phys. Rev. B **73**, 132102 (2006).

[21] M. J. Verstraete, Phases of Polonium via Density Functional Theory, Phys. Rev. Lett. **104**, 035501 (2010).

[22] C.-J. Kang, K. Kim, and B. I. Min, Phonon softening and superconductivity triggered by spin-orbit coupling in simple-cubic α-polonium crystals, Phys. Rev. B **86**, 054115 (2012).

[23] L. E. Díaz-Sánchez, A. H. Romero, and X. Gonze, Phonon band structure and interatomic force constants for bismuth: Crucial role of spin-orbit interaction, Phys. Rev. B **76**, 104302 (2007).

[24] A. Dal Corso, Ab initio phonon dispersions of face centered cubic Pb: Effects of spin-orbit coupling, J. Phys.: Condens. Matter **20**, 445202 (2008).

[25] J. Donohue, *The Structures of the Elements* (Wiley, New York, 1974).

[26] D. A. Young, *Phase Diagrams of the Elements* (University of California Press, Berkeley, 1991).

[27] S. Schönecker, X.-Q. Li, K. Koepernik, B. Johansson, L. Vitos, and M. Richter, Metastable cubic and tetragonal phases of transition metals predicted by density-functional theory, RSC Adv. **5**, 69680 (2015).

[28] G. Grimvall, *Thermophysical Properties of Materials* (Elsevier, Amsterdam, 1999).

[29] J. F. Nye, *Physical Properties of Crystals: Their Representation by Tensors and Matrices* (Oxford University Press, Oxford, 1960).

[30] L. Fast, J. M. Wills, B. Johansson, and O. Eriksson, Elastic constants of hexagonal transition metals: Theory, Phys. Rev. B **51**, 17431 (1995).

[31] V. Vítek, Intrinsic stacking faults in body-centred cubic crystals, Philos. Mag. A **18**, 773 (1968).

[32] M. Jo, Y. M. Koo, B.-J. Lee, B. Johansson, L. Vitos, and S. K. Kwon, Theory for plasticity of face-centered cubic metals, Proc. Natl. Acad. Sci. U.S.A. **111**, 6560 (2014).

[33] P. E. Blöchl, Projector augmented-wave method, Phys. Rev. B **50**, 17953 (1994).

[34] G. Kresse and D. Joubert, From ultrasoft pseudopotentials to the projector augmented-wave method, Phys. Rev. B **59**, 1758 (1999).

[35] G. Kresse and J. Furthmüller, Efficient iterative schemes for *ab initio* total-energy calculations using a plane-wave basis set, Phys. Rev. B **54**, 11169 (1996).

[36] See Supplemental Material at http://link.aps.org/supplemental/10.1103/PhysRevB.97.224305 for the numerical parameters for total energy and phonon calculations, the phonon dispersion relations and density of states for the metastable hcp phases, the effect of SOC on phonon dispersion relations of hcp Ir and Au, the Fermi surface of hcp Pt, and the structural relaxation effect during the hcp to fco displacive transformation.

[37] J. P. Perdew, K. Burke, and M. Ernzerhof, Generalized Gradient Approximation Made Simple, Phys. Rev. Lett. **77**, 3865 (1996).

[38] J. P. Perdew and Y. Wang, Accurate and simple analytic representation of the electron-gas correlation energy, Phys. Rev. B **45**, 13244 (1992).

[39] F. Tran, R. Laskowski, P. Blaha, and K. Schwarz, Performance on molecules, surfaces, and solids of the Wu-Cohen GGA exchange-correlation energy functional, Phys. Rev. B **75**, 115131 (2007).

[40] A. Dal Corso, Ab initio phonon dispersions of transition and noble metals: Effects of the exchange and correlation functional, J. Phys.: Condens. Matter **25**, 145401 (2013).

[41] S. Steiner, S. Khmelevskyi, M. Marsmann, and G. Kresse, Calculation of the magnetic anisotropy with projected-augmented-wave methodology and the case study of disordered $Fe_{1-x}Co_x$ alloys, Phys. Rev. B **93**, 224425 (2016).

[42] G. Lehmann and M. Taut, On the numerical calculation of the density of states and related properties, Phys. Status Solidi B **54**, 469 (1972).

[43] A Togo and I Tanaka, First principles phonon calculations in materials science, Scr. Mater. **108**, 1 (2015).

[44] K. Lejaeghere, G. Bihlmayer, T. Björkman, P. Blaha, S. Blügel, V. Blum, D. Caliste, I. E. Castelli, S. J. Clark, A. Dal Corso, S. de Gironcoli, T. Deutsch, J. K. Dewhurst, I. Di Marco, C. Draxl, M. Dułak, O. Eriksson, J. A. Flores-Livas, K. F. Garrity, L. Genovese, P. Giannozzi, M. Giantomassi, S. Goedecker, X. Gonze, O. Grånäs, E. K. U. Gross, A. Gulans, F. Gygi, D. R. Hamann, P. J. Hasnip, N. A. W. Holzwarth, D. Iuşan, D. B. Jochym, F. Jollet, D. Jones, G. Kresse, K. Koepernik, E. Küçükbenli, Y. O. Kvashnin, I. L. M. Locht, S. Lubeck, M. Marsman, N. Marzari, U. Nitzsche, L. Nordström, T. Ozaki, L. Paulatto, C. J. Pickard, W. Poelmans, M. I. J. Probert, K. Refson, M. Richter, G.-M. Rignanese, S. Saha, M. Scheffler, M. Schlipf, K. Schwarz, S. Sharma, F. Tavazza, P. Thunström, A. Tkatchenko, M. Torrent, D. Vanderbilt, M. J. van Setten, V. Van Speybroeck, J. M. Wills, J. R. Yates, G.-X. Zhang, and S. Cottenier, Reproducibility in density functional theory calculations of solids, Science **351**, aad3000 (2016).

[45] Z.-L. Liu, J.-H. Yang, L.-C. Cai, F.-Q. Jing, and D. Alfè, Structural and thermodynamic properties of compressed palladium: *Ab initio* and molecular dynamics study, Phys. Rev. B **83**, 144113 (2011).

[46] N. A. Smirnov, Ab initio calculations of the elastic and thermodynamic properties of gold under pressure, J. Phys.: Condens. Matter **29**, 105402 (2017).

[47] J. X. Zheng-Johansson, O. Eriksson, and B. Johansson, Systematic behavior of the hexagonal axial ratio for the *d* transition metals, Phys. Rev. B **59**, 6131 (1999).

[48] F. Ducastelle and F. Cyrot-Lackmann, Moments developments: II. Application to the crystalline structures and the stacking fault energies of transition metals, J. Phys. Chem. Solids **32**, 285 (1971).

[49] X. Li and S. Schönecker, First-principles prediction of the stacking fault energy of gold at finite temperature, Acta Mater. **135**, 88 (2017).

[50] R. A. Robie and J. L. Edwards, Some Debye temperatures from single-crystal elastic constant data, J. Appl. Phys. **37**, 2659 (1966).

[51] S. Rajasekhara, K. J. Ganesh, K. Hattar, J. A. Knapp, and P. J. Ferreira, Evidence of metastable hcp phase grains in as-deposited nanocrystalline nickel films, Scr. Mater. **67**, 189 (2012).

[52] J. Higuchi, M. Ohtake, Y. Sato, T. Nishiyama, and M. Futamoto, Preparation and structural characterization of hcp and fcc Ni

epitaxial thin films on Ru underlayers with different orientations, Jpn. J. Appl. Phys. **50**, 063001 (2011).

[53] L. N. Brewer, D. M. Follstaedt, K. Hattar, J. A. Knapp, M. A. Rodriguez, and I. M. Robertson, Competitive abnormal grain growth between allotropic phases in nanocrystalline nickel, Adv. Mater. (Weinheim, Ger.) **22**, 1161 (2010).

[54] J. L. Huang, Z. Li, H. H. Duan, Z. Y. Cheng, Y. D. Li, J. Zhu, and R. Yu, Formation of hexagonal-close packed (hcp) rhodium as a size effect, J. Am. Chem. Soc. **139**, 575 (2017).

[55] X. Huang, S. Li, Y. Huang, S. Wu, X. Zhou, S. Li, C. L. Gan, F. Boey, C. A. Mirkin, and H. Zhang, Synthesis of hexagonal close-packed gold nanostructures, Nat. Commun. **2**, 292 (2011).

[56] H. Wormeester, E. Hüger, and E. Bauer, hcp and bcc Cu and Pd films, Phys. Rev. Lett. **77**, 1540 (1996).

[57] H. Wormeester, M. E. Kiene, E. Hüger, and E. Bauer, Growth of hcp Cu on W(100), Surf. Sci. **377**, 988 (1997).

[58] P. Villars and L. D. Calvert, *Pearson's Handbook of Crystallographic Data for Intermetallic Phases*, 2nd ed. (ASM International, Materials Park, OH, 1991), Vol. 4.

[59] B. Fultz, Vibrational thermodynamics of materials, Prog. Mater. Sci. **55**, 247 (2010).

[60] J. M. Ziman, *Eletrons and Phonons: The Theory of Transport Phenomena in Solids* (Clarendon, Oxford, 1960).

[61] E. B. Tadmor and N. Bernstein, A first-principles measure for the twinnability of FCC metals, J. Mech. Phys. Solids **52**, 2507 (2004).

[62] H. Van Swygenhoven, P. M. Derlet, and A. G. Frøseth, Stacking fault energies and slip in nanocrystalline metals, Nat. Mater. **3**, 399 (2004).

[63] B. Q. Li, M. L. Sui, and S. X. Mao, Twinnability predication for fcc metals, J. Mater. Sci. Technol. **27**, 97 (2011).

[64] Z. H. Jin, S. T. Dunham, H. Gleiter, H. Hahn, and P. Gumbsch, A universal scaling of planar fault energy barriers in face-centered cubic metals, Scr. Mater. **64**, 605 (2011).

[65] A. Hunter, R. F. Zhang, and I. J. Beyerlein, The core structure of dislocations and their relationship to the material surface, J. Appl. Phys. **115**, 134314 (2014).

[66] X.-Z. Wu, R. Wang, S.-F. Wang, and Q.-Y. Wei, Ab initio calculations of generalized-stacking-fault energy surfaces and surface energies for FCC metals, Appl. Surf. Sci. **256**, 6345 (2010).

[67] S. Kibey, J. B. Liu, D. D. Johnson, and H. Sehitoglu, Predicting twinning stress in fcc metals: Linking twin-energy pathways to twin nucleation, Acta Mater. **55**, 6843 (2007).

[68] L. E. Murr, *Interfacial Phenomena in Metals and Alloys* (Addison-Wesley, London, 1975).

[69] P. C. J. Gallagher, The influence of alloying, temperature, and related effects on the stacking fault energy, Metall. Trans. **1**, 2429 (1970).

[70] C. L. Tracy, S. Park, D. R. Rittman, S. J. Zinkle, H. Bei, M. Lang, R. C. Ewing, and W. L. Mao, High pressure synthesis of a hexagonal close-packed phase of the high-entropy alloy CrMnFeCoNi, Nat. Commun. **8**, 15634 (2017).

[71] F. Zhang, Y. Wu, H. Lou, Z. Zeng, V. B. Prakapenka, E. Greenberg, Y. Ren, J. Yan, J. S. Okasinski, X. Liu, Y. Liu, Q. Zeng, and Z. Lu, Polymorphism in a high-entropy alloy, Nat. Commun. **8**, 15687 (2017).

[72] Z. Li, K. G. Pradeep, Y. Deng, D. Raabe, and C. C. Tasan, Metastable high-entropy dual-phase alloys overcome the strength-ductility trade-off, Nature (London) **534**, 227 (2016).

[73] P. J. H. Denteneer and W. van Haeringen, Stacking-fault energies in semiconductors from first principles calculations, J. Phys. C **20**, L883 (1987).